# Multi-scale in situ mechanical investigation of the superelastic behavior of a Cu–Al–Be polycrystalline shape memory alloy

Younes El Hachi, Sophie Berveiller, Boris Piotrowski, Jonathan Paul Wright, Wolfgang Ludwig, Benoît Malard

# Multi-scale *in situ* mechanical investigation of the superelastic behavior of a Cu–Al–Be polycrystalline shape memory alloy

Y. El Hachi[a], S. Berveiller[a,*], B. Piotrowski[a], J. Wright[b], W. Ludwig[c], B. Malard[d]

[a] LEM3, Arts et Métiers Institute of Technology, CNRS, Université de Lorraine, HESAM Université, 4, rue Augustin Fresnel, Metz 57070, France
[b] ESRF-EBS, 71 avenue des Martyrs, Grenoble 38000, France
[c] MATEIS, 345 Avenue Gaston Berger, Villeurbanne 69100, France
[d] CIRIMAT, CNRS, INPT, UPS, Université de Toulouse, 4 Allée Emile Monso, Toulouse 31030, France

ARTICLE INFO

*Keywords:*
3D high-energy synchrotron X-ray diffraction
Martensitic transformation
Shape memory alloy
Internal stress
Finite element modeling

ABSTRACT

The superelastic behavior of a Cu–Al–Be alloy was studied *in situ* during tensile tests combining two high-energy synchrotron techniques. The initial microstructure was reconstructed using diffraction contrast tomography; the elastic strain and stress tensors of each individual grain were then determined using a 3D X-ray diffraction microscopy technique. The alloy was heat-treated until coarse grains formed, and the probed volume fraction was limited to ~ 200 grains. The mean grain size, as estimated from both techniques, agreed well with that determined by optical microscopy, i.e., approximately 130 μm. During the early stage of the martensitic transformation (MT), 187 grains with strong stress heterogeneities were detected in the elastic domain; in particular, the stress values along the tensile direction varied by a factor of three between different grains. The reconstructed 3D microstructure served as input data for finite element modeling, wherein a micromechanical approach factoring in the martensitic transformation was used to simulate the *in situ* tensile tests. The coupled numerical and experimental tensors of the 187 grains confirmed strong stress heterogeneities between them. The influence of the position and crystallographic orientation of the neighboring grains were also examined.

## 1. Introduction

Owing to their particular thermomechanical behaviors, shape memory alloys (SMAs) are increasingly being used in industrial applications under extreme operating conditions (aerospace, offshore plants, etc.). During mechanical loading, austenite undergoes a stress-induced martensitic transformation (MT) to martensite, resulting in the phenomenon of superelasticity. This transformation can be reversed during unloading; the recoverable strain is approximately 3% in polycrystalline materials, and up to 10% in single crystals [1]. The actuation stress and the recoverable strain depend on microstructural features, such as the martensitic transformation starting temperature ($M_s$), grain size [2], and the crystallographic orientation of the grains [1,3]. This dependency is even stronger in Cu-based alloys, owing to their highly anisotropic elastic behavior [4] and large Zener ratio (~13, calculated from single-crystal elastic constants), which is among the highest for metals. Therefore, their microstructural features play a key role in optimizing their mechanical behavior, thus necessitating a "material-by-design" approach. However, such an approach requires a better understanding of the relationship between the microstructural features and the mechanical properties at the grain scale.

To predict this superelastic behavior, several models have been developed at different metallurgical scales using macroscopic phenomenological approaches or micromechanical approaches; however, the transition scale method significantly improves the accuracy of the intragranular field predictions. Accordingly, most phenomenological models consider only a few internal variables to describe the MT mechanism, without factoring in the crystallographic parameters of the activated martensite variant plane [5–7]. These models consider the alloy as an equivalent homogeneous medium without grain boundaries, and their predictions for the macroscopic tension, compression, and torsion results generally agree well with the experimental results [8]. As such, micromechanical models must be adopted to predict the effects of the local mechanical fields on the intergranular stress. Based on the crystallographic structure of the alloy, one internal variable is defined for each martensite habit plane variant, and their evolution (thermally or mechanically induced) depends on the interaction system. Nevertheless, the resolution of these models is time-consuming and induces size limitations for the studied microstructure [9,10].

* Corresponding author.
*E-mail address:* sophie.berveiller@ensam.eu (S. Berveiller).

https://doi.org/10.1016/j.actamat.2022.118107

Moreover, few of these models have been validated at the grain scale owing to the lack of available experimental data.

Over the last two decades, 3D grain mapping techniques using synchrotron radiation have been developed to analyze polycrystalline materials [11]. Among them, 3D X-ray diffraction microscopy (3DXRD) allows determining the position of the center of mass of individual grains in bulk specimens, as well as their average elastic strain and stress tensors and crystallographic orientations [12]. In addition, the diffraction contrast tomography (DCT) method enables time-lapse observations of 3D grain structures [13] and intragranular orientation fields [14] with a spatial resolution of approximately 1 μm. Coupled with finite element modeling (FEM), this technique has been used to study plastic slip activity in Al–Li [14] and Zr–Ti polycrystals [15]. In addition, Sedmak et al. [16] studied the internal stress field distribution during the stress-induced MT in a Ni–Ti polycrystalline wire, observing that a localized deformation front propagated through the samples. However, limited experimental data are available on the behavior of Cu–Al–Be alloys at the grain scale. In a previous study [17], the crystallographic orientation of four grains was measured during *in situ* tensile testing. Their rotation increased, and the austenite split into sub-domains as it experienced the MT, which was reversed during unloading. El Hachi et al. [18] were able to record the elastic strain and stress tensors of 100 grains. After conducting a statistical analysis, they concluded that the grain stress level depends on the grain location (with grains at the surface being less constrained) and orientation. More recently, Paranjape et al. [19] observed the same trend in a polycrystalline Ni–Ti SMA and used their experimental data as the input for FEM to define the synthetic microstructure. Although they considered only an anisotropic elastic constitutive law in their numerical approach, their results highlighted the role of heterogeneity in the intragranular stress during the occurrence of MT. As the MT mechanism was not included in their model, the comparison between the experimental data and numerical results was limited to the very early stage of the transformation.

This study aimed to investigate the microstructural features and the occurrence of superelasticity in a Cu-based SMA at the grain scale. Datasets from two experimental techniques, 3DXRD and DCT, were coupled to establish a FEM micromechanical model that effectively considers the role of MT. The experimental microstructure, determined by DCT calculations, served as input data for FEM. Subsequently, the individual grain behavior was independently calculated for the 187 grains of the probed volume fraction. The numerical results were then compared with the 3DXRD experimental data, while factoring in the elastic strain and stress tensors.

## 2. Materials and methods

### 2.1. Materials and sample preparation

The Cu–Al–Be SMA was provided by NIMESIS Technology (France); its weight composition was 87.9% copper, 11.5% aluminum, and 0.6% beryllium, with an austenitic microstructure at room temperature ($M_s = -100$ °C). The specimen was a cylindrical wire with a diameter of 0.86 mm, and it was thermally treated at 700 °C for 5 min to reduce the number of grains in the gage volume and to facilitate DCT and 3DXRD data analysis. The average grain size was also measured using optical microscopy.

### 2.2. DCT and 3DXRD data processing

DCT (Fig. 1a) was used to determine the initial microstructure of the gage volume, while the 3DXRD measurements (Fig. 1b) were recorded during an *in situ* tensile test (Fig. 1c). These experiments were carried out at the Materials Science Beamline, ID11, at the European Synchrotron Radiation Facility (EBS-ESRF). A 1000 × 700 $\mu m^2$ (Hor. × Vert.) monochromatic X-ray beam (E = 65.3 keV, Hf = edge) was used to illuminate the sample, which was mounted on the rotation stage. During $\omega$-axis rotation (perpendicular to the incident beam direction), different grains and Miller planes were analyzed by the diffraction beam. The DCT and 3DXRD methods measurements were performed in two stages. In the first stage, the initial microstructure of the sample was characterized without the tensile machine to obtain a complete rotation ($\omega$-range = 360°) of the sample. In the second stage, the tensile machine was used to characterize the sample, which was limited to 220° for the 3DXRD experiments during the *in situ* loading. The $\omega$-step, $\delta\omega$, was 0.1° and 0.25° for the DCT and 3DXRD analyses, respectively. A diffraction image was acquired at each $\omega$ (exposure time = 0.15 s) using 2D Fast Readout Low Noise (FReLoN) detectors (developed at the ESRF) set perpendicularly to the incident beam. The near-field detector for DCT had an effective pixel size of 1.56 $\mu m^2$ and was placed 8 mm downstream of the sample, while the far-field detector for 3DXRD had an effective pixel size of 47.2 $\mu m^2$ and was 242 mm downstream. The experimental setup geometry was calibrated using a $CeO_2$ calibration powder.

The far-field 3DXRD and DCT image processing is described in Appendix A. The strain resolution is frequently quoted to be $10^{-4}$ in the 3DXRD literature [21], which gives a stress accuracy varying between ± 2 and ± 23 MPa from grain to grain, as the Young's modulus varies between 21 and 228 GPa for the present alloy. Error bars and standard errors are not included in this work because such errors would alter the values to some extent; however, the overall trends and conclusions remain the same.

### 2.3. In situ *3DXRD tensile test*

After characterizing the initial microstructure (as described in Section 2.2), the sample was placed in a 5 kN ADMET load frame, which was mounted on the rotation stage. The gage length was 33 mm. The beam size was increased to a height of 1 mm to ensure that all austenitic grains in the initial microstructure (700 μm high) remained under the beam area throughout the *in situ* measurements. Uniaxial tensile loading was performed (tensile direction aligned with the $\omega$-axis). The tensile curve and loading steps, spread out between the elastic and MT domains, are shown in Fig. 1c (measurements during unloading are not discussed here). This load frame recorded the longitudinal displacement between the grips of the tensile machine rather than the local displacement near the probed area. Therefore, the tensile slope in the elastic domain was then adjusted using the FEM calculation based on the mechanical model of elasticity. A small stress relaxation can be observed during each *in situ* 3DXRD scan, as shown in Fig. 1c. The 3DXRD data were acquired after stabilization, and a 3DXRD scan was performed at each load step to characterize the evolution of the elastic strain, stress, and orientation in all individual grains.

The peak search process described in Appendix A was performed at each loading step. Only peaks arising from the austenitic phase were indexed, because the emerging small domains of martensite produced weak peaks (in contrast to austenite), rendering the crystallographic analysis of the complex monoclinic martensite structure (M18R) a challenging task.

### 2.4. Finite element simulation

The Neper software package was used to create a mesh from the voxelated DCT reconstruction [22,23]. A detailed description of the process can be found in Appendix B. After performing convergence tests, quadratic tetrahedral elements (Abaqus© C3D10) were chosen.

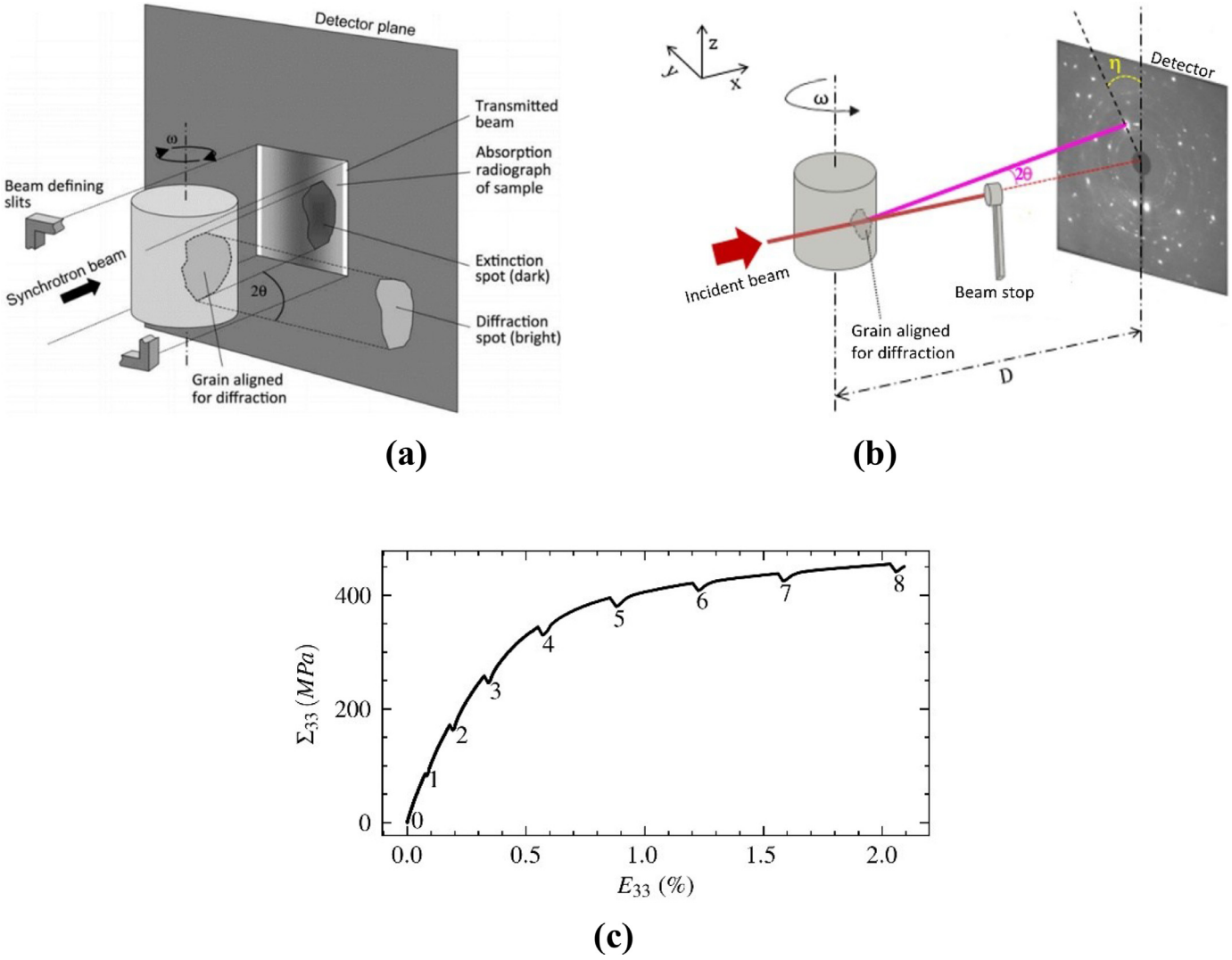


**Fig. 1.** Experimental methods. Schematics of the (a) DCT [20] and (b) 3DXRD setups [20]. (c) Superelastic tensile curve along with the nine *in situ* loading steps (0 to 8).

To simulate the superelastic behavior, a micromechanical model based on the definition of a local thermodynamic potential was used [10,24]. This model was multivariant: volume fractions, $f^n$, from the 24 different variants of martensite were used to describe the internal state rather than a phenomenological model with an average or single-variant fraction. Although the constitutive law of such a model is derived from single crystals, the use of FEM makes it compatible with multiple crystals. Quantities such as the elastic strain tensor $\overline{\overline{\varepsilon^e}}$, transformation strain tensor $\overline{\overline{\varepsilon^{tr}}}$, stress tensor $\overline{\overline{\sigma}}$, and volume fraction of the martensite variants $f^n$ were obtained from the FEM simulation for each element in the mesh and at each load increment. Considering the volume of each element, the above quantities were also averaged for each individual grain for a mesoscopic analysis and comparison with the *in situ* 3DXRD results. Owing to numerical constraints, the FEM simulation was only performed to a macroscopic strain of 1.1%, which was sufficient to study the first stages of MT.

## 3. Results

### 3.1. Initial microstructure

A total of 187 grains were obtained in the gage volume during the DCT experiment (Fig. 2a) and digitized using the Neper software package for further FEM calculations, as presented in Section 2.4 (Fig. 2c). The equivalent grain size was calculated from the volume of the grains by assuming spherical grains. The resulting mean grain size was 120 µm, which was in good agreement with the optical measurements (approximately 130 µm). The microstructure was then compared to that obtained from the 3DXRD measurements (Fig. 2b), and the individual grain volume was estimated based on the median intensity of the {400} peaks indexed to each austenite grain, which were the most intense peaks after being corrected by Lorentz factors. This method assumes that the grain-to-sample ratio of the diffracted intensity is equal to the grain-to-sample volume ratio [12].

The DCT and 3DXRD datasets of the initial microstructure were matched and compared, considering the misorientations and Euclidean distances between centroids. Very good overall agreement was obtained between the DCT and 3DXRD calculations: for instance, the highest observed misorientation was 0.1°, which corresponded to the integration step $\delta\omega$ used in the DCT experiment.

The initial microstructure was further analyzed, mostly using the 3DXRD data, to identify the austenite unit cell and investigate the possible correlations between the different features of the microstructure. Notable differences arose between the surface and bulk grains. In Fig. 3b, the size and completeness of the diffraction of each grain are plotted versus the normal coordinates of the

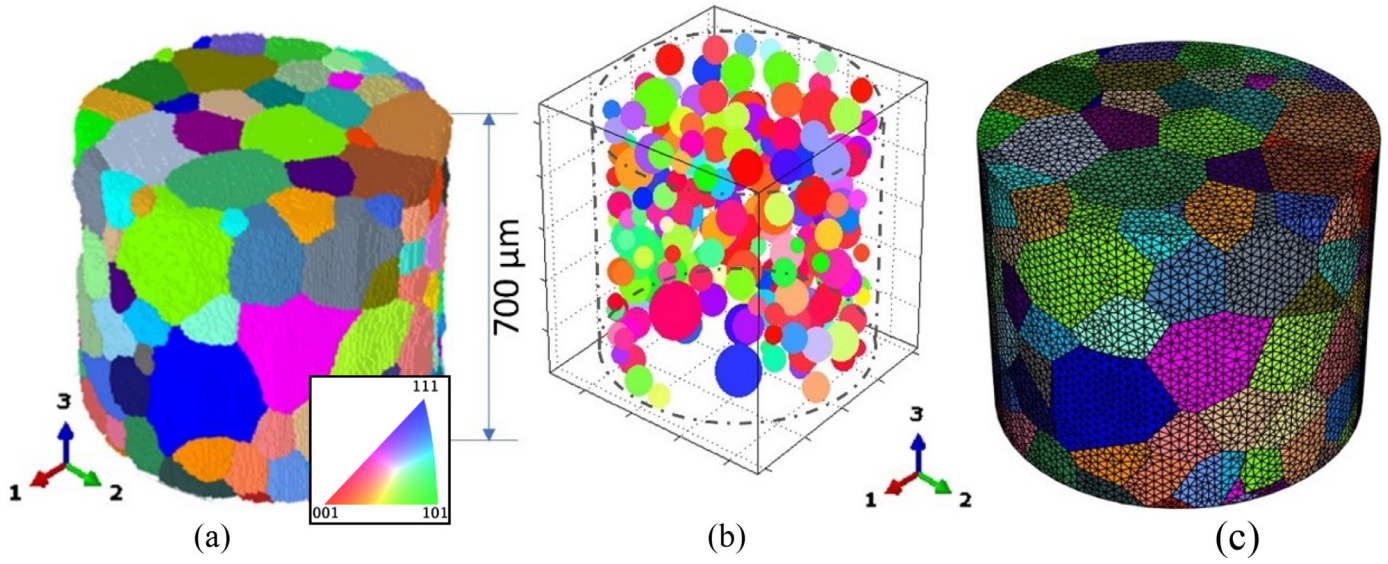


**Fig. 2.** Representations of the initial microstructure obtained by (a) DCT and (b) 3DXRD. The center of each sphere is the center of mass of the corresponding grain, its diameter is the grain size, and its color is the crystallographic orientation with respect to the axis of the cylindrical specimen. (c) FEM-generated microstructure mesh.

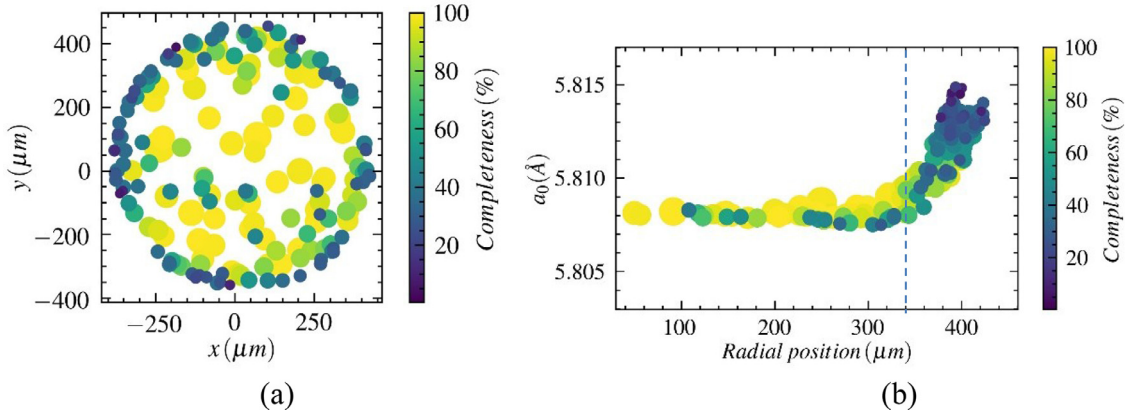


**Fig. 3.** Indexing of the grains at the initial loading state. (a) Projection of the grain position along the sample axis. (b) Distribution of the lattice parameter vs distance of the grain centroid from the sample axis. The circle size is proportional to the grain size, while the color indicates the completeness of the grain.

grains (projection of the centroids over the plane normal to the rotation axis). Grains observed in the bulk were coarser than grains near the outer surface. The grain size gradient may be a result of the drawing process and subsequent thermal treatment. Likewise, the completeness (ratio between numbers of obtained and obtainable unique reflections) of the bulk grains was close to 100%, which was twice that of the surface grains. This was consistent with the previous results, as small grains can produce weak diffraction intensities that are below the detection threshold during the 3DXRD peak-search routine.

Finally, the unit cell parameter, $a_0$, of each grain was plotted as a function of the radial position (Fig. 3b), that is, the radial distance to the sample axis ($\omega$-axis). The mean $a_0$ value for the bulk grains (radial distance $<$ 340 µm) was 5.808 $\pm$ 0.001 Å, whereas it varied between 5.810 and 5.815 Å for the surface grains. These larger unit cells were theoretically ascribed either to a chemical composition gradient or to the generation of mechanical stress during the drawing process. The origin of the disparities between the surface and bulk grains will be further investigated in future studies. However, in the present study, the initial unit cell of each austenitic grain was used as the reference non-strained unit cell, $a_0$, to calculate the elastic strain tensor during tensile loading. Therefore, the residual strain was not considered.

### *3.2. Superelastic tensile loading*

#### *3.2.1. 3DXRD data analysis*

The 3DXRD diffraction images were processed as described in Section 2.2. While the data processing is straightforward in the case of an undeformed single-phase polycrystal (i.e., the initial state), difficulties arise as the MT starts to proceed. Fig. 4a and b show the 3DXRD images at the initial loading state and at loading state 6, respectively. The diffraction spots arising from the unstrained austenite (Fig. 4a) shifted and broadened over the $2\theta$ diffraction rings as a result of lattice rotation and elastic strain (Fig. 4b). They also became weaker, and their intensity spread over the successive $\omega$ images because of the growth of martensitic domains. At loading state 7 and beyond, the diffraction images increasingly exhibited overlapping intensities owing to the increased martensite volume fraction. As a result, the overlapped spots were no longer considered when indexing austenite. Starting from loading state 7, even more grains could no longer be indexed; only a limited number of diffraction spots from low-numbered {hkl} families could be appropriately segmented, which was insufficient for adequate indexing. The experimental parameters and data reduction procedure had to be adjusted to account for such effects at higher loading levels. Moreover, we noticed from the indexing step

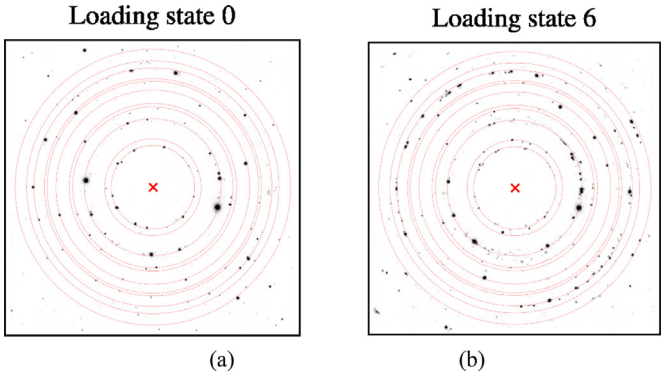


**Fig. 4.** 3DXRD diffraction image obtained for the Cu–Al–Be alloy at the same point during the (a) initial loading state and (b) loading state 6. Images for all loading steps are given in Appendix D. Red dotted circles indicate austenite diffraction positions.

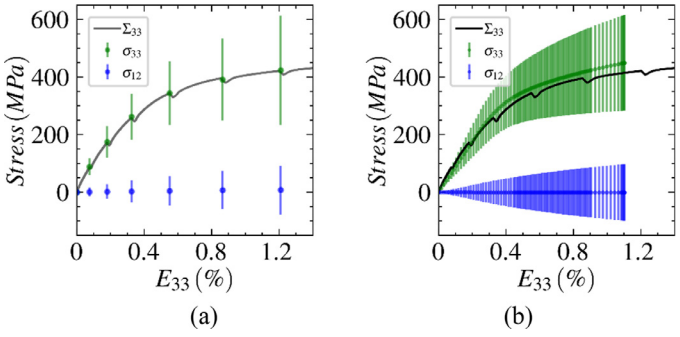


**Fig. 5.** Representation of the macroscopic stress, the stress component along tensile direction 3, and the shear stress component of the 187 grains as a function of the macroscopic strain: (a) experimental values and (b) FEM values. Errors bars constitute the standard deviation for the 187 grains.

that some austenite grains began to split into several orientations at higher loadings. This grain- splitting phenomenon was also observed in a previous study [17]; indeed, the occurrence of subdomains has been related to the formation of martensite plates inside the initial austenite grains, as a specific orientation formed from each side of martensite plates. Upon unloading, the plates disappeared as the martensite disappeared, and austenite rotated back to its initial orientation. The present analysis focused only on the first six loadings ($E_{33} < 1.2\%$), that is, when the 187 initial grains could still be tracked confidently in both the elastic domain (loading states 0 to 3) and the transformation domain (loading states 4 to 6).

### 3.2.2. Macroscopic scale results (187 grains)

The stress tensor $\overline{\overline{\sigma}}$ was calculated for the 187 grains at each loading step using the experimental elastic strain tensor $\overline{\overline{\varepsilon^e}}$ and the stiffness tensor (**Table 1, Appendix C**). Here, direction 3 was aligned with the tensile direction, and direction 1 was aligned with the incident beam. Fig. 5a shows the evolution of the axial stress components ($\sigma_{33}$), the shear stress ($\sigma_{12}$) of the 187 grains, and the macroscopic stress ($\Sigma_{33}$) plotted as functions of macroscopic strain.

First, the mean mechanical behavior of the 187 tracked grains (green circles) was observed to be consistent with the macroscopic applied stress (solid line). For example, at $E_{33} = 1.21\%$, the average $\overline{\sigma_{33}}$ value was 423 MPa for an applied stress value of $\Sigma_{33} = 416$ MPa. All the other mean stress values (axial and shear components) ranged between − 4 and 8 MPa (only the evolution of $\sigma_{12}$ was plotted for readability). Thus, the tensile response in the gage volume (0.7 mm high) was representative of the whole sample (effective length of 33 mm), and uniaxial macroscopic loading was achieved. However, a heterogeneous stress distribution was observed, which was already present in the elastic domain and increased along with the MT evolution. For instance, at loading state 6 ($E_{33} = 1.21\%$, $\Sigma_{33} = 416$ MPa), some grains exhibited stress as high as 600 and as low as 200 MPa. These results indicate a highly heterogeneous mechanical response in the austenitic grains, which is further discussed in Section 4.

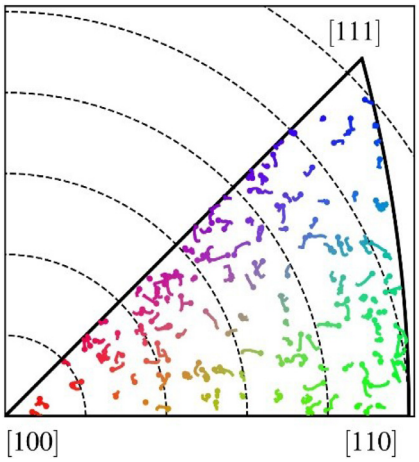


**Fig. 6.** IPF map of crystallographic orientation along tensile direction 3 for all the 187 grains. Dots represent the initial position, whereas lines indicate the evolution during loading.

For comparison, the stress tensor $\overline{\overline{\sigma}}$ was determined from the FEM simulation for each mesh element and at each load increment. The element-related output data were integrated over each grain, considering the volume of its elements. The FEM simulation was run only up to a macroscopic strain of 1.1%. Fig. 5b presents the FEM results for the $\sigma_{33}$ axial stress and $\sigma_{12}$ shear stress components for the 187 grains, as well as the macroscopic stress ($\Sigma_{33}$) versus the macroscopic strain. The general trend agreed well with the experimental observations, considering the mean values for the axial and shear stresses: the simulated $\overline{\sigma_{33}}$ value was very close to the macroscopic applied value, while all the other stress components were relatively negligible. Thus, the FEM results confirmed the strong heterogeneity in the intergranular stress values both qualitatively and quantitatively.

### 3.2.3. Stress distribution at the mesoscopic scale (grain scale)

First, the evolution of the crystallographic orientation was determined experimentally and plotted in inverse pole figure (IPF) map (Fig. 6) along tensile direction 3 for the 187 grains. As observed in a previous study [17], no clear trend appeared: grains located near the same pole did not seem to rotate toward the same final position. This was attributed to the austenite rotation, which was mainly related to the formation of martensite plates separating misoriented regions of austenite within one grain. The FEM results could not be compared because the model did not provide access to that rotational parameter. Therefore, in the following section, only the strain and stress are quantified and discussed at the grain scale.

The experimentally observed lattice strain and stress for all grains along the tensile direction at loading state 6 are presented in the IPF maps in Fig. 7a and 7b, respectively.

It should be noted that residual stress was not considered in the initial loading state, implying that the observed stress developed only during loading. A clear correlation between the strain-stress state and the crystallographic orientation is shown in Fig. 7: grains near the <100> plane exhibited high $\varepsilon^e_{33}$ and low $\sigma_{33}$ values, while grains near the <111> plane showed low $\varepsilon^e_{33}$ and high $\sigma_{33}$ val-

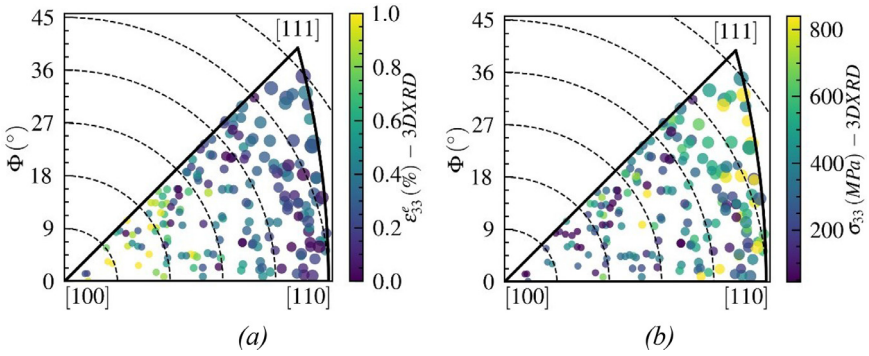


**Fig. 7.** IPF maps along the tensile direction of the lattice (a) strain and (b) stress in the 187 austenite grains at loading state 6.

ues. This was consistent with the fact that <100> grains have been confirmed to be susceptible to transformation, while <111> grains show the opposite behavior [1]. However, here, some grains did not follow this general rule, as some similar orientations with respect to the loading direction could significantly differ in terms of $\varepsilon^e_{33}$ and $\sigma_{33}$ values, as can be observed near the <111> pole. These results confirm the observations of a Ni–Ti SMA reported by Paranjape et al. [19]: the grain response to stress is heterogeneous even for similar orientations. Therefore, other microstructural features must also be considered to better understand the mechanism underlying this phenomenon.

## 4. Discussion

Both the experimental (Fig. 5a) and numerical (Fig. 5b) stress analyses, performed at the macroscopic and mesoscopic scales, clearly established the heterogeneous response of austenite grains during superelastic loading. Such intergranular heterogeneities were observed in the elastic domain as well as during the MT. This may have been due to (1) the effects of the initial microstructure (distribution of orientation, location, and size of austenitic grains), which are intensified by the high elastic anisotropy of the Cu–Al–Be alloy, and/or (2) the intergranular or intragranular interactions as martensite developed within the grain. These effects are discussed in the following sections.

### 4.1. Influence of orientation

To further analyze the individual grain behavior, the experimental and numerical results for the individual stress evolution of each of the 187 grains were independently compared. First, a focused analysis of three coarse bulk grains with different orientations was conducted.

A pseudo-Schmid factor, relative to the MT, was calculated for each grain orientation considering the habit plane normal and shear direction of each variant. The Young's modulus along the tensile direction, $E_3$, was calculated from the elastic constants and the crystallographic orientation of the grain. The Euler angles, maximum pseudo-Schmid factor $SF^{max}$ relative to the MT, and Young's modulus $E_3$ in the loading direction of the three grains are given in Table 1. Grain 1 had an orientation close to <100> with respect to the loading direction, which is generally regarded as a direction along which transformation is easy, with a high pseudo-Schmid factor. In contrast, Grains 2 and 3 were oriented closer to <111>, which is known to be more resistant to transformation, and therefore exhibited a low pseudo-Schmid factor.

**Table 1**
Orientation in the tensile direction, Euler angles, maximum pseudo-Schmid factor relative to the MT ($SF^{max}$), and Young's modulus in the loading direction $E_3$ for the three grains.

| | Orientation | ($\phi$1,$\Phi$,$\phi$2) (°) | $SF^{max}$ | $E_3$ (GPa) |
|---|---|---|---|---|
| Grain 1 | ≈ [100] | (−71.5, 9.2, 110.3) | 0.49 | 22 |
| Grain 2 | ≈ [545] | (−36.4, 51.3, 52.0) | 0.18 | 185 |
| Grain 3 | ≈ [757] | (26.3, 50.5, −54.0) | 0.20 | 168 |

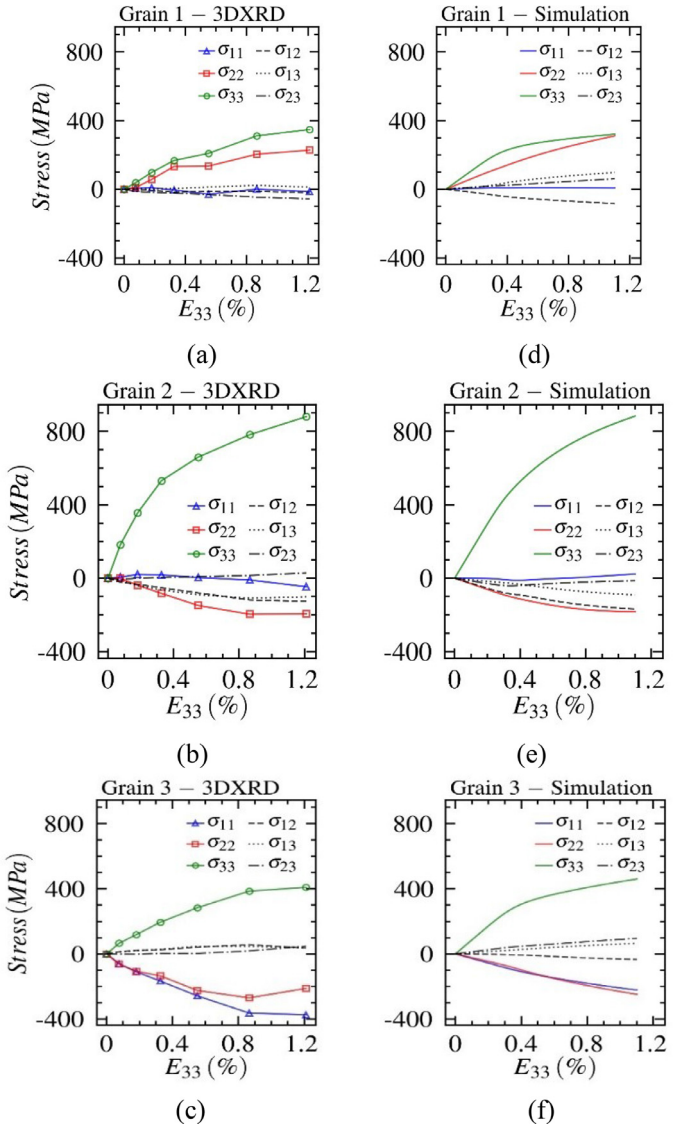


**Fig. 8.** Evolution of the six components of the elastic stress tensor in Grains 1, 2, and 3 vs the macroscopic strain, as obtained by the 3DXRD (a, b, c) and FEM (d, e, f) measurements.

Fig. 8 presents the evolution of the six components of the elastic stress tensor as determined by 3DXRD (**a–c**) or calculated by FEM (**d–f**). As shown in Fig. 8a, Grain 1 had a lower axial stress, $\sigma_{33}$, than the two other grains, from the elastic domain; values in Grain 2 were 2.5 times higher at a macroscopic strain $E_{33} = 0.8\%$, with respective values of $\sigma_{33}$ of 300 and 780 MPa. Moreover, Grain 1 developed another axial tensile stress of the same magnitude as $\sigma_{33}$; in contrast, at least one compressive axial stress occurred in Grains 2 and 3. The shear components remained quite weak; Grain 2, the hardest component, presented the highest value (approximately −100 MPa at $E_{33} = 0.8\%$). This confirmed that although the crystallographic orientation is a key factor affecting a grain's properties under every stress state, it also verified that two similarly oriented grains can behave differently. Even under uniaxial macroscopic loading, grains behave as if in a complex multi-axial loading owing to several factors, such as the specific grain environment and position in the sample. Therefore, it becomes difficult to detect the onset of MT at the grain scale using the evolution of the stress tensor. This information can be more effectively obtained from the FEM results.

The numerical stress tensors of the three grains are plotted in Fig. 8d–f. As a first qualitative observation, the stress–strain trends for all axial and shear stress components given by the FEM calculations were noticeably similar to the experimental ones (Fig. 8a–c) for the three grains. This comparison was extended over all 187 grains, and less than 16% of all stress tensor components differed from their corresponding experimental values by more than 100 MPa, including grains near the surface and grains at the FEM boundary conditions. This disparity may have had different origins. In fact, the tessellation and meshing operations from the DCT mapping process resulted in an idealization of the grain boundaries (Fig. 2c) with the presence of sharp edges, triple points, and even quadruple points in the geometric boundaries. These meshing shortcomings locally increase the stress values and therefore the sample average stress, especially at high loading. Moreover, the model did not consider plasticity, which could influence the stress values. Regardless of these issues and the experimental accuracy, one can conclude that the micromechanical model can capture the mechanical behavior of the alloy at the macroscopic and grain scales in the low-MT domain. The model was then used to study the effect of the alloy's microstructural features on the onset of MT at the intragranular scale.

### 4.2. MT and variant selection

The volume fractions $f^n$ of the 24 crystallographic martensite variants ($n = 1$ to 24) were included in the thermomechanical model as internal variables and computed by the FEM at each integration point. In addition, the variant activation was predicted through a local thermodynamic potential. The volume fractions $f^n$ were averaged for each austenite grain, considering the volume of the meshing elements, for intergranular analysis. Their evolution is presented in Fig. 9a as a function of macroscopic strain for Grain 1, along with the pseudo-Schmid factor for MT. Five variants were activated successively, all corresponding to high pseudo-Schmid factors, so the material seemed to obey Schmid's law, as defined for

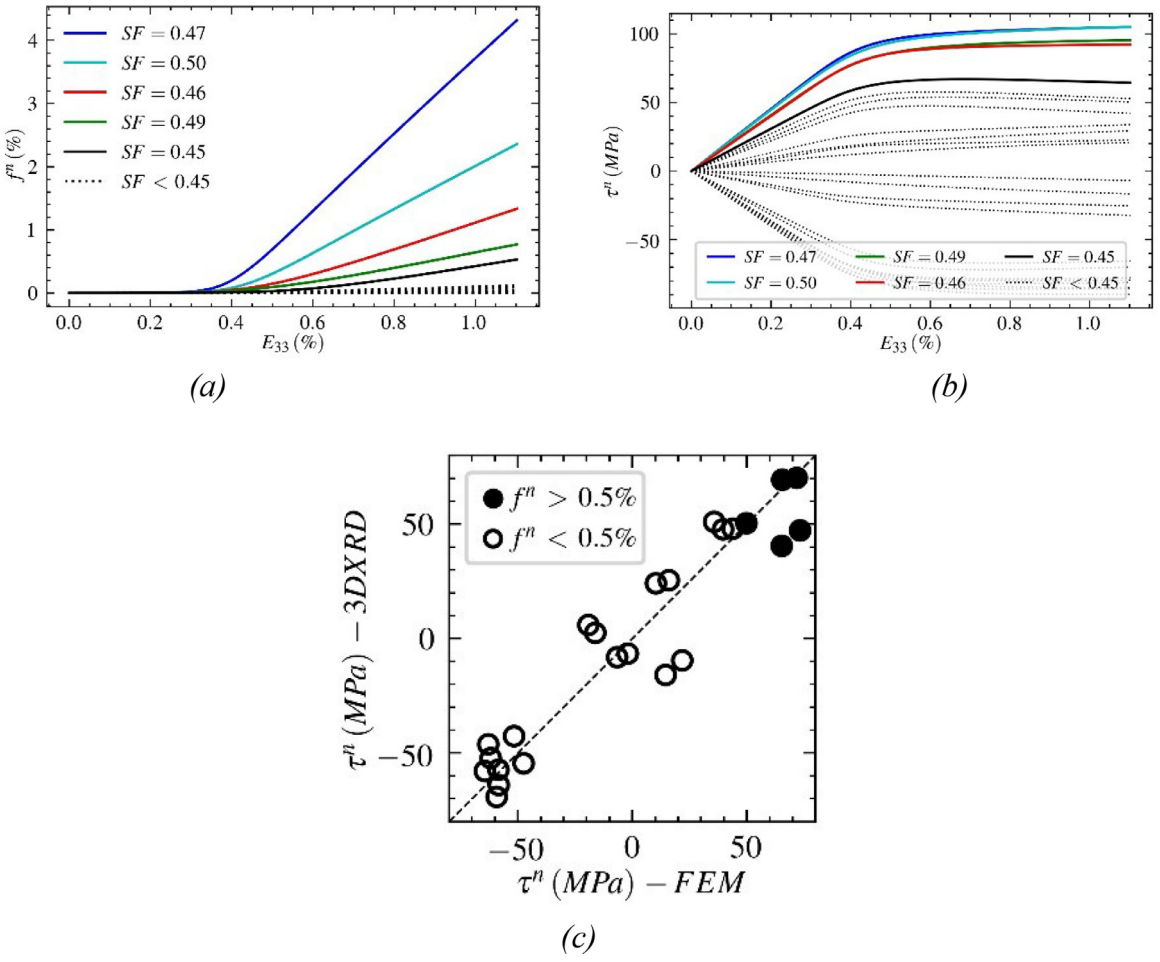


**Fig. 9.** Grain 1 (a) evolution of the 24 martensite variant fractions during loading; (b) evolution of the 24 resolved shear stresses calculated from FEM; (c) experimentally resolved shear stresses vs numerically calculated stresses at loading state 4 ($E_{33} = 0.55\%$); black dots correspond to variants with a volume fraction higher than 0.5%.

the single-crystal case. The first variant appeared at $E_{33} = 0.3\%$, and its pseudo-Schmid factor was 0.47, which was not the highest one reported here; in order of activation during the loading sequence, the pseudo-Schmid factors were 0.47, 0.50, 0.46, 0.49, and 0.45. Their development also differed as the MT proceeded: the first variant was also the one with the higher final martensite fraction, whereas the last one, appearing from $E_{33} = 0.6\%$, did not evolve significantly.

The resolved shear stress was calculated for each variant using the simulation stress state averaged over the grain (Fig. 9b), and this stress was compared to the values obtained using the experimental stress state (Fig. 9c); in the latter case, the grain rotation was considered so that the crystallographic orientation was updated at each loading point. In Fig. 9b, the activated and non-activated martensite variants are shown by solid and dashed lines, respectively. Among all possible variants, the activated ones clearly exhibited higher resolved shear stress after the elastic domain. These values continually increased up to approximately loading state 5 ($E_{33} = 0.5\%$), where they tended to saturate. The first two activated variants had a maximum resolved shear stress of approximately 100 MPa. The next two showed slightly lower values, while the fifth saturated at approximately 65 Mpa. As a first observation, these values were in very good agreement with those determined using the experimental stress tensor (Fig. 9c), although the rotation of austenitic grains was not included in the FEM computation of the resolved shear stress. This agreement implied that although the diffraction data did not provide a complete description of the martensite phase, the most accurate variants could still be predicted from the experimental data (3DXRD) by deriving and comparing the 24 shear stress scalars at each loading step. However, the maximum values did not enable the determination of the critical value, which should not depend on the grain orientation; instead, all grains should share a common value. Therefore, further insight is necessary when observing the shear stress at a finer microstructure scale.

To confirm that the material seemed to obey or not the Schmid's law, the variant selection was investigated for Grain 2, which was harder than Grain 1. Owing to its <111> orientation with respect to the loading direction, it exhibited smaller pseudo-Schmid factors ranging between 0.01 and 0.18. The 24 volume fractions of the martensite variants in this grain are shown in Fig. 10a.

Although Grain 2 is difficult to transform because of its crystallographic orientation, it began to transform under the same macroscopic strain as Grain 1: two variants, "Var 18″ and "Var 11," were activated at $E_{33} = 0.3\%$ and developed further to reach 8% and 4% volume fractions, respectively, at the end of the FEM calculation. Further, the pseudo-Schmid factors for Var 18 and Var 11 (0.18 and 0.17, respectively) were the highest among the 24 possible variants, which agreed with the results for Grain 1. However, a third variant, Var 19, was also activated, despite its very low pseudo-Schmid factor (0.02) at a macroscopic strain of $E_{33} = 0.6\%$. Its intragranular microstructure and mechanical state were therefore studied to understand the onset of this transformation.

The location of each activated variant within Grain 2 is shown in Fig. 10b. The variant with the highest pseudo-Schmid factor, Var 11, developed along a grain boundary and propagated within the grain to a limited extent. Var 18 developed from two opposite grain boundaries, where higher fractions of martensite were observed. In contrast, Var 19, which developed later, was rather concentrated in a single region that was apparently shared with Var 18; this seemed to be also the case for Var 11 and Var 18 in the left corner of the grain. This finding suggested that the development of a well-oriented martensite variant may eventually be accompanied by the localized growth of a martensite variant with a weaker "pseudo-Schmid" factor to better accommodate the local stress field, which is in agreement with the findings of Paranjape

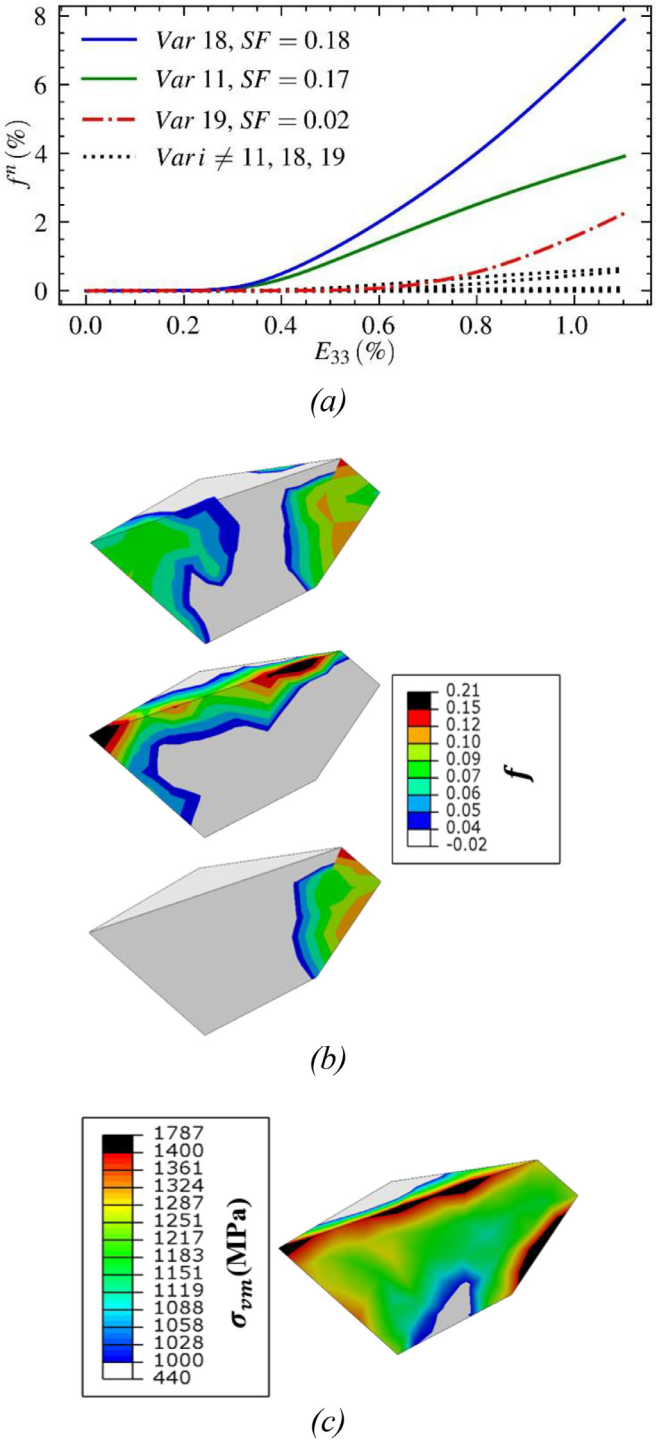


**Fig. 10.** Grain 2. (a) Evolution of the 24 volume fractions of the martensite variants at loading state 6; (b) Location of activated variants 18, 11, and 19 (from top to bottom) within the grain at loading state 6; (c) von Mises stress map.

and Anderson [25]. Fig. 10c shows a plot of the von Mises stress distribution, $\sigma_{vm}$, which was chosen even when grains were in a multi-axial stress state as it provided a clear view of the intragranular stress heterogeneity. Indeed, a high stress concentration was observed particularly in the regions of the grain boundaries where the MT had occurred to a greater extent. This clearly showed that the activation of martensite variants was not only governed by the orientation effect but was also very sensitive to intergranular stress heterogeneities in the polycrystal structure. While a mesoscopic

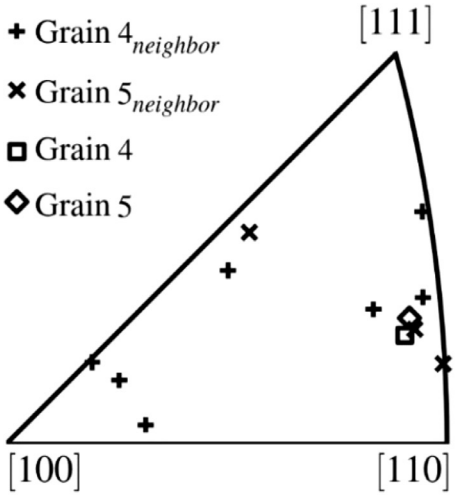


(a)

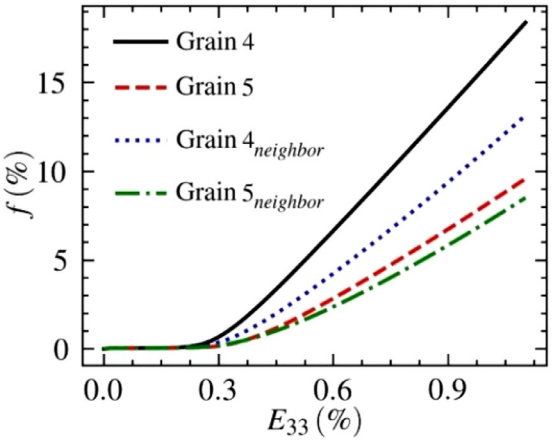


(b)

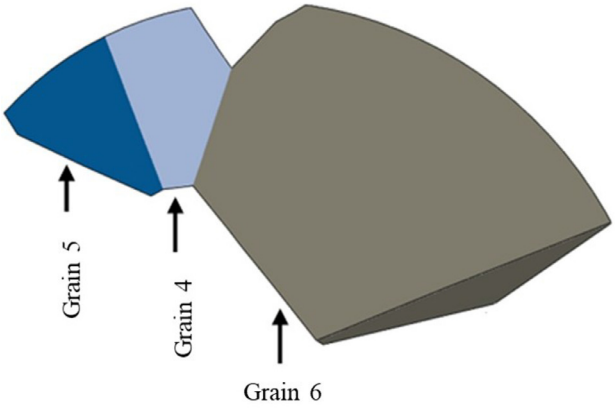


(c)

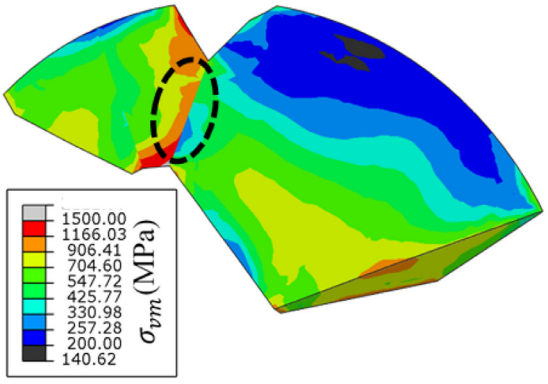


(d)

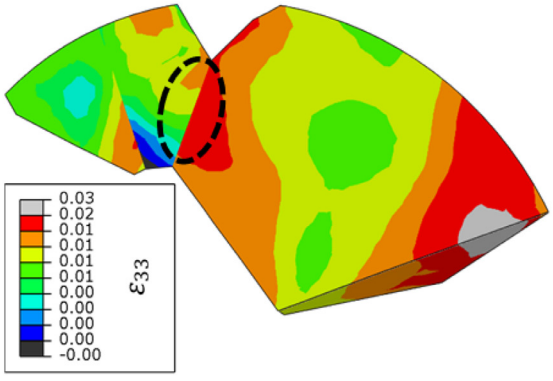


(e)

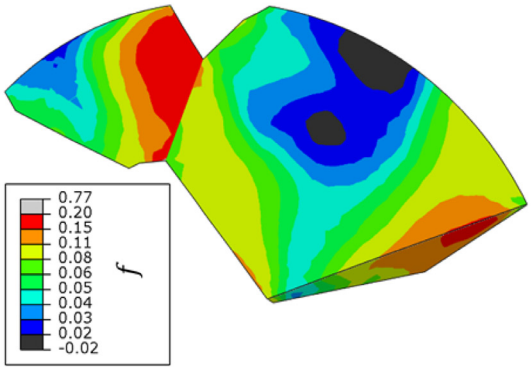


(f)

**Fig. 11.** Simulated spatial distribution of stress, strain, and phase fractions in selected polycrystal grains in loading state 6 (E33 = 1.1%). (a) Orientation of the tensile axis direction in austenite grains; (b) evolution of the martensite volume fraction in grains; (c) Grains 4–6 within the austenitic microstructure; (d) spatial distribution of von Mises stress within Grains 4–6; (e) spatial distribution of the total strain component $\varepsilon_{33}$ in the tensile direction within Grains 4–6; (f) martensite volume fraction within Grains 4–6.

description of the mechanical behavior could provide the first prediction, it is essential to consider the effects of local stress on the microstructural evolution of superelastic SMA polycrystals. Finally, very high stress values were observed; even if these values were not realistic, they qualitatively demonstrated how heterogeneous the local behavior was, despite the FEM only being concerned with the first stage of MT with a maximum macroscopic strain of 1.1%. Therefore, the model could be improved by including a plasticity criterion for the austenite phase in particular to avoid such high von Mises stress values, as Paranjape et al. did for Ni–Ti alloys [25].

### *4.3. Interaction with neighboring austenite grains*

To compare the influence of the neighboring grains, two adjacent grains (Grains 4 and 5) were selected based on the DCT reconstruction model; they were similar in size, which corresponded to the average grain size in the sample, and were located in a similar place in the sample, both being near the surface. Their orientation was nearly identical and located near the <110> pole, as shown in the IPF (Fig. 11a); their maximum "pseudo-Schmid" factors were also similar at 0.36 and 0.35, respectively. All these common features mitigated the generation of biases owing to their contribution to stress heterogeneity.

In addition, these two grains shared a significant volume of common neighboring orientations that were identified by the DCT calculations; the intersection of their neighboring grain volume was equal to 74%. Grains in contact with only Grain 4 or Grain 5 were labeled as "exclusive neighbors." The orientation of these exclusive neighboring grains of Grains 4 and 5 is shown in Fig. 11a. Three of the seven exclusive neighboring grains of Grain 4 were oriented near <100>, while Grain 5 exhibited relatively similar orientations with two out of its three exclusive neighboring grains.

The evolution of the martensite volume fraction for Grains 4 and 5, as calculated by FEM, is presented in Fig. 11b. Despite their common features, the onset of MT and its development were evidently not similar in the two grains. In Grain 4, the MT started at a macroscopic strain of $E_{33} = 0.25\%$, and the final martensite volume fraction was 18% at $E_{33} = 1.1\%$. Grain 5 began to transform later ($E_{33} = 0.35\%$) and reached a maximum martensite volume fraction of only 10%. The rotation of each grain was also calculated from the 3DXRD experimental data; at $E_{33} = 1.1\%$, Grain 4 rotated by 0.35° from its initial position, while Grain 5 rotated by 0.5° . Bucsek et al. [26] used dark-field X-ray microscopy at the ESRF on a single-crystal Ni–Ti SMA to study the lattice strain and rotations as a function of the distance to the austenite/martensite interface during cooling. They found that the austenite phase located close to the interface exhibited high lattice strain, which constrained its ability to rotate. The exact opposite behavior was observed away from the interface. Therefore, they inferred that this phenomenon also occurs under stress-induced MT, and the 3DXRD technique in the present study was able to capture it at the grain scale.

The MT evolution of the neighboring grains is also presented in Fig. 11b. MT started earlier and reached higher values in the exclusive neighboring grains of Grain 5 compared to those of Grain 4. The maximal martensite volume fraction of the two grains reached 13% and 9%, respectively. The orientations of the exclusive neighboring grains of Grain 4 were close to the <100> pole, which is highly susceptible to transformation.

The influence of the exclusive neighboring grains was then studied at a finer scale. A 2D slice of both grains of interest, as well as of a favorably oriented neighboring grain of Grain 4 (labeled Grain 6), is presented in Fig. 11c. The latter was the largest among the neighboring grains. The von Mises stress distribution, $\sigma_{vm}$, is plotted in Fig. 11d. Grain 5 exhibited a quite homogeneous stress distribution, averaged at 600 MPa. This was not the case for Grain 4, where the stress values were low near the boundary with Grain 5 (400 MPa) and increased when moving toward the well-oriented grain, where they reached a maximum of 800 MPa. A strong stress disparity was observed at the grain boundary: on one side of the boundary, the stress was approximately 450 MPa (Grain 6), while on the other side, the stress value reached as high as 900 MPa (Grain 4). Although this value was arguably very high (especially when considering that the factor of plasticity was not considered in this model), it is significant for stress to concentrate in that region. This stress concentration led to a localized MT in Grain 4: a high volume fraction of martensite (up to 20%) appears in the zone with high von Mises stress; conversely, it is only 5–6% in the low-von-Mises-stress zone. The MT evolution in Grain 5 was more homogeneous, which was in agreement with the stress distribution. Paranjape et al. [25] observed the same phenomenon in a Ni–Ti SMA using a micromechanical FEM calculation. Despite their simplified description of the grain morphology, they assessed the effect of the neighboring grain environment on the development of MT: in-plane neighboring grains that are easy to transform can more easily transfer tensile stress to the parent grain, thereby promoting MT. On the other hand, an environment of difficult-to-transform in-plane neighboring grains less effectively transfers compressive stress, thus inhibiting the MT of the parent grain. These effects are more pronounced in Cu-based SMAs than in Ni–Ti ones because of their higher elastic anisotropy, which induces more stress variation. Moreover, the magnitude of stress transferred among the in-plane neighboring grains is proportional to their axial strain mismatches [15]. As shown in Fig. 11e, the <100> neighboring grains possessed a high axial strain component, $\varepsilon_{33}$, near the boundary with Grain 4, resulting in a high strain incompatibility and transferring a large amount of internal stress.

## 5. Conclusion

The superelastic behavior of a Cu-based SMA was investigated at the grain scale during an *in situ* tensile test using high-energy synchrotron measurements. The 3DXRD technique effectively illustrated the grain-averaged orientation, stress tensor, and grain volume. Accordingly, DCT measurements indicated the grain positions in the sample, along with their shape and neighboring grain environment. The stress state of most grains was mainly influenced by their crystallographic orientation: as a general trend, the highest and lowest stress values were observed in grains oriented along the <111> and <100> tensile directions, respectively. However, some grains did not follow this rule; similarly-oriented grains exhibited stress values that differed by a factor of three. These heterogeneities were confirmed by a FEM simulation, wherein the DCT data were used as input data, and a micromechanical law taking into account the MT was implemented in Abaqus©. The model was validated by comparing the stress tensors of all 187 individual grains in the polycrystal, and the numerical results corresponded well with the experimental results. This outcome highlighted the influence of the neighboring grains on the MT evolution in similarly oriented grains: easy-to-transform grains generally promoted MT near the grain boundary in a hard-to-transform grain, influencing its average stress state.

## Declaration of Competing Interest

None.


## Acknowledgments

This work was supported by the Region Grand Est (France) – Agreement 2016–7978. The authors would like to thank the European Synchrotron Radiation Facility (ESRF) for beam time allo-

cations under proposal MA3379. We would also like to thank Dr. R. Quey (Mines de Saint Etienne, France) for his help in the DCT reconstruction, Dr. Mame Daro Fall for her help in analyzing the 3DXRD data, and Prof. Yves Chemisky (Université de Bordeaux, France) for his improvements to the SIMCOON library.

## Supplementary materials

Supplementary material associated with this article can be found, in the online version, at doi:10.1016/j.actamat.2022.118107.

## References

[1] H. Horikawa, S. Ichinose, T. Morii, K. Otsuka, Orientation dependence of $\beta_1 \rightarrow \beta_1'$ stress-induced martensite transformation in a Cu-Al-Ni alloy, Metall. Trans. A 19 (1988) 915–923, doi:10.1007/BF02628376.

[2] M. Sade, F. de Castro Bubani, F.C. Lovey, V. Torra, Effect of grain size on stress induced martensitic transformations in a Cu–Al–Be polycrystalline shape-memory alloy. Pseudoelastic cycling effects and microstructural modifications, Mater. Sci. Eng. A 609 (2014) 300–309, doi:10.1016/j.msea.2014.05.018.

[3] P. Šittner, P. Lukáš, V. Novák, M.R. Daymond, G.M. Swallowe, *In situ* neutron diffraction studies of martensitic transformations in NiTi polycrystals under tension and compression stress, Mater. Sci. Eng. A 378 (2004) 97–104, doi:10.1016/j.msea.2003.09.112.

[4] D. Rios-Jara, S. Belkahla, A. Canales, H. Flores, G. Gunenin, Elastic constant measurements of ~Cu-Al-Be alloys, Scr. Metall. Mater. 25 (1991) 1351–1355.

[5] Y. Chemisky, A. Duval, E. Patoor, T.Ben Zineb, Constitutive model for shape memory alloys including phase transformation, martensitic reorientation and twins accommodation, Mech. Mater. 43 (2011) 361–376, doi:10.1016/j.mechmat.2011.04.003.

[6] C. Lexcellent, E. Gibeau, A short review of shape memory alloys thermomechanical models, Solid State Phenom. 138 (2008) 355–366, doi:10.4028/www.scientific.net/SSP.138.355.

[7] D. Lagoudas, D. Hartl, Y. Chemisky, L. Machado, P. Popov, Constitutive model for the numerical analysis of phase transformation in polycrystalline shape memory alloys, Int. J. Plast. 32–33 (2012) 155–183, doi:10.1016/j.ijplas.2011.10.009.

[8] P. Sittner, L. Heller, J. Pilch, P. Sedlak, M. Frost, Y. Chemisky, A. Duval, B. Piotrowski, T. Ben Zineb, E. Patoor, F. Auricchio, S. Morganti, A. Reali, G. Rio, D. Favier, Y. Liu, E. Gibeau, C. Lexcellent, L. Boubakar, D. Hartl, S. Oehler, D.C. Lagoudas, J.V. Humbeeck, Roundrobin SMA modeling, in: Proceedings of the 8th European Symposium on Martensitic Transformations, Prague, Czech Republic, EDP Sciences, 2009, p. 08001, doi:10.1051/esomat/200908001.

[9] T. Merzouki, C. Collard, N. Bourgeois, T. Ben Zineb, F. Meraghni, Coupling between experiment and numerical simulation of shape memory alloy multicrystal, in: Proceedings of the 8th European Symposium on Martensitic Transformations, Prague, Czech Republic, EDP Sciences, 2009, p. 06035, doi:10.1051/esomat/200906035.

[10] E. Patoor, A. Eberhardt, M. Berveiller, Micromechanical modelling of superelasticity in shape memory alloys, J. Phys. IV 06 (1996) FranceC1-277-C1-292, doi:10.1051/jp4:1996127.

[11] H.F. Poulsen, Multi scale hard X-ray microscopy, Curr. Opin. Solid State Mater. Sci. 24 (2020) 100820, doi:10.1016/j.cossms.2020.100820.

[12] H.F. Poulsen, The 3DXRD Microscope, in: H.F. Poulsen (Ed.), Three-Dimensional X-Ray Diffraction Microscopy: Mapping Polycrystals and Their Dynamics, Springer, Berlin, Heidelberg, 2004, pp. 89–94, doi:10.1007/978-3-540-44483-1_8.

[13] W. Ludwig, S. Schmidt, E.M. Lauridsen, H.F. Poulsen, X-ray diffraction contrast tomography: a novel technique for three-dimensional grain mapping of polycrystals. I. Direct beam case, J. Appl. Crystallogr. 41 (2008) 302–309, doi:10.1107/S0021889808001684.

[14] L. Renversade, R. Quey, W. Ludwig, D. Menasche, S. Maddali, R.M. Suter, A. Borbély, Comparison between diffraction contrast tomography and high-energy diffraction microscopy on a slightly deformed aluminium alloy, IUCrJ 3 (2016) 32–42, doi:10.1107/S2052252515019995.

[15] H. Abdolvand, J. Wright, A.J. Wilkinson, Strong grain neighbour effects in polycrystals, Nat. Commun. 9 (2018) 171, doi:10.1038/s41467-017-02213-9.

[16] P. Sedmak, P. Sittner, J. Pilch, C. Curfs, Evolution of internal stresses during cyclic superelastic deformation of NiTi investigated by X-ray synchrotron, Mater. Today Proc. 2 (2015) S731–S734, doi:10.1016/j.matpr.2015.07.386.

[17] S. Berveiller, B. Malard, J. Wright, E. Patoor, G. Geandier, *In situ* synchrotron analysis of lattice rotations in individual grains during stress-induced martensitic transformations in a polycrystalline CuAlBe shape memory alloy, Acta Mater. 59 (2011) 3636–3645, doi:10.1016/j.actamat.2011.02.037.

[18] Y.E. Hachi, B. Malard, S. Berveiller, J. Wright, Measurement of lattice rotations and internal stresses in over one hundred individual grains during a stress-induced martensitic transformation, MATEC Web Conf. 33 (2015) 02003, doi:10.1051/matecconf/20153302003.

[19] H.M. Paranjape, P.P. Paul, H. Sharma, P. Kenesei, J.-S. Park, T.W. Duerig, L.C. Brinson, A.P. Stebner, Influences of granular constraints and surface effects on the heterogeneity of elastic, superelastic, and plastic responses of polycrystalline shape memory alloys, J. Mech. Phys. Solids 102 (2017) 46–66, doi:10.1016/j.jmps.2017.02.007.

[20] W. Ludwig, P. Reischig, A. King, M. Herbig, E.M. Lauridsen, G.C. Johnson, T.J. Marrow, J.Y. Buffière, Three-dimensional grain mapping by X-ray diffraction contrast tomography and the use of Friedel pairs in diffraction data analysis, Rev. Sci. Instrum. 80 (2009) 033905, doi:10.1063/1.3100200.

[21] H. Sharma, R.M. Huizenga, S.E. Offerman, A fast methodology to determine the characteristics of thousands of grains using three-dimensional X-ray diffraction. I. Overlapping diffraction peaks and parameters of the experimental setup, J. Appl. Crystallogr. 45 (2012) 693–704, doi:10.1107/S0021889812025563.

[22] R. Quey, P.R. Dawson, F. Barbe, Large-scale 3D random polycrystals for the finite element method: generation, meshing and remeshing, Comput. Methods Appl. Mech. Eng. 200 (2011) 1729–1745.

[23] R. Quey, L. Renversade, Optimal polyhedral description of 3D polycrystals: method and application to statistical and synchrotron X-ray diffraction data, Comput. Methods Appl. Mech. Eng. 330 (2018) 308–333.

[24] D. Chatziathanasiou, Y. Chemisky, G. Chatzigeorgiou, F. Meraghni, Modeling of coupled phase transformation and reorientation in shape memory alloys under non-proportional thermomechanical loading, Int. J. Plast. 82 (2016) 192–224, doi:10.1016/j.ijplas.2016.03.005.

[25] H. Paranjape, P.M. Anderson, Texture and grain neighborhood effects on Ni–Ti shape memory alloy performance, Model. Simul. Mater. Sci. Eng. 22 (2014) 075002, doi:10.1088/0965-0393/22/7/075002.

[26] A. Bucsek, H. Seiner, H. Simons, C. Yildirim, P. Cook, Y. Chumlyakov, C. Detlefs, A.P. Stebner, Sub-surface measurements of the austenite microstructure in response to martensitic phase transformation, Acta Mater. 179 (2019) 273–286, doi:10.1016/j.actamat.2019.08.036.